

ORIGINAL ARTICLE

Open Access



Analytical Modelling and Experiment of Novel Rotary Electro-Mechanical Converter with Negative Feedback Mechanism for 2D Valve

Bin Meng, Mingzhu Dai, Chenhang Zhu, Chenchen Zhang, Chuan Ding* and Jian Ruan

Abstract

The manufacturing of spiral groove structure of two-dimensional valve (2D valve) feedback mechanism has shortcomings of both high cost and time-consuming. This paper presents a novel configuration of rotary electro-mechanical converter with negative feedback mechanism (REMC-NFM) in order to replace the feedback mechanism of spiral groove and thus reduce cost of valve manufacturing. In order to rapidly and quantitatively evaluate the driving and feedback performance of the REMC-NFM, an analytical model taking leakage flux, edge effect and permeability non-linearity into account is formulated based on the equivalent magnetic circuit approach. Then the model is properly simplified in order to obtain the optimal pitch angle. FEM simulation is used to study the influence of crucial parameters on the performance of REMC-NFM. A prototype of REMC-NFM is designed and machined, and an exclusive experimental platform is built. The torque-angle characteristics, torque-displacement characteristics, and magnetic flux density in the working air gap with different excitation currents are measured. The experimental results are in good agreement with the analytical and FEM simulated results, which verifies the correctness of the analytical model. For torque-angle characteristics, the overall torque increases with both current and rotation angle, which reaches about 0.48 N·m with 1.5 A and 1.5°. While for torque-displacement characteristics, the overall torque increases with current yet decreases with armature displacement due to the negative feedback mechanism, which is about 0.16 N·m with 1.5 A and 0.8 mm. Besides, experimental results of conventional torque motor are compared with counterparts of REMC-NFM in order to validate the simplified model. The research indicates that the REMC-NFM can be potentially used as the electro-mechanical converter for 2D valves in civil servo areas.

Keywords: Electro-mechanical converter, Magnetic circuit topology, Analytical modeling, 2D valve

1 Introduction

Servo valves have functions of both electro-mechanical energy conversion and signal amplification, which, to a great extent, determines overall performance of electro-hydraulic control system itself [1–4]. The electro-hydraulic servo valve can be divided into direct acting type and pilot operated type. The former features simple structure

and good anti-pollution ability, but the main disadvantage is that the driving force of the electro-mechanical converter is limited, which is not suitable for high pressure and large flow situation [5–7]. In order to overcome the Bernoulli force and obtain the ideal static and dynamic characteristics, servo valve usually need to be designed as a multi-stage structure with pilot-operated mechanism. Typical pilot-operated servo valves include nozzle flapper valve, jet pipe valve, voice coil servo valve, two-dimensional valve, etc. The nozzle flapper valve has complex structure, high processing and assembly

*Correspondence: chuanding1986@163.com

College of Mechanical Engineering, Zhejiang University of Technology, Hangzhou 310023, China

accuracy, and poor anti-pollution ability owing to pilot control stage structure [8–10]; The jet pipe valve has excellent anti-pollution ability, but the jet characteristics are not easy to be predicted [11, 12]; The moving coil servo valve has a large volume, and the power to weight ratio is not ideal, which is mainly used in industrial servo occasions.

Two-dimensional valve (2D valve), firstly proposed by Ruan in 1989, is a novel pilot-operated valve based on the principle of hydraulic servo-screw mechanism, whose spool moves in both horizontal and rotary motion, and the two movements are in a fixed proportional relationship similar to mechanical screw [13–15]. Unlike other servo valves, this valve integrates the separated pilot stage and power stage onto one single spool, and has no tiny hole or slot structure that is liable to be blocked like nozzle flapper valve. Therefore, it possesses advantages of extremely simple structure and excellent anti-pollution capability [16, 17]. Recently it has been used in military, aerospace, construction machinery and other mobile hydraulic applications where high power to weight ratio is being put for priority. However, 2D valve requires manufacturing of special and complicated geometric features such as the spiral groove on valve sleeve. And it usually requires EDM (electrical-discharge machining) machine tool with at least three axes, which is not only expensive but also time consuming. This shortcoming greatly influences the further promotion of 2D valve for industry servo area that is more sensitive to cost and relatively less sensitive to performance [18]. Therefore, necessary structural changes need to be considered in order to reduce machining cost.

One of the feasible ways is to integrate the feedback function into the electro-mechanical converter (EMC) so that the complicated spiral groove might be simplified. 2D valve needs a rotary electro-mechanical converter (REMC) to rotate spool firstly in order to actuate the so-called “2D” mechanism. Based on different operation principle, the REMCs can be divided into voice coil motor (VCM), torque motor and rotary proportional solenoid (RPS). The VCM features high linearity, large stroke, and excellent dynamic characteristics with large currents [19, 20]. Nevertheless, large currents cause serious heating problem, which usually requires additional cooling measures. For example, for the moving coil servo valve used by Hitachi for steel rolling equipment the compressed air is used for forcible heat dissipation. In order to reduce the excitation level, Wu et al. proposed a novel VCM where a Halbach array is designed to improve flux density of working air gap [21]. The RPS was originated from its linear counterpart which features flat torque-angle characteristics. It has large thrust force and is easy to be designed as a “wet type” actuator with high-pressure oil

resistant ability [22, 23]. The difficulties for design of RPS lie that there is no such a general approach like welding a magnetic isolation ring to obtain proportional control features. Several studies have been conducted on novel magnetic circuit topology and parameter optimization to achieve the flat torque-angle curve [24]. Torque motor has advantages of high control accuracy and fast dynamic response, which has been widely used as EMC of several servo valves including nozzle-flapper valve, jet pipe valve and deflector jet pipe valve. However, it has shortcomings of having some precise mechanical and electrical parts, which actually sacrifice simplicity, set-up and manufacturing costs. Zhang et al. proposed a novel torque motor with hybrid-magnetization pole arrays, whose output torque can be increased by range of 47%–52% compared with traditional designs, while maintaining the original size [25]. In order to solve self-excited oscillation issue of servo valve, Li et al. added magnetic fluid into the working air gap of torque motor and found that magnetic fluids can improve the stability of torque motor and the dynamic response of the whole valve [26, 27]. For actual situation the torque motors might have unequal air gaps due to production errors. Urata studied the influence of such unequal thickness on the output torque of torque motor [28]. Liu et al. proposed a novel analytical model counting the influence of magnetic reluctance of magnetic elements on torque motor that could provide reference for the controller design of servo valve [29]. Recently, functional materials such as piezoelectric crystal [30], giant magnetostrictive material [31], magnetorheological fluid and shape memory alloy are adopted as EMC by some novel servo valves [32, 33], which usually possess extremely fast dynamic characteristics. However, these materials are liable to be influenced by temperature variation and nonlinear hysteresis. Also, they depend on the material deformation to obtain the displacement, which makes them more suitable for linear EMC.

So far, all valve EMCs in the existing literatures only have single function to drive armature (mover) to move. EMC with both driving and feedback mechanisms has not been reported yet. This paper presents a novel REMC integrated with negative feedback mechanism (REMC-NFM) in order to replace the feedback mechanism of spiral groove of traditional 2D valve. The advantage of such arrangement is that a simple rectangular sensing groove can be used to replace the complicated spiral sensing groove, which can greatly reduce manufacturing cost.

The rest of this paper is organized as follows: In Section 2, the configuration and working principle of REMC-NFM is introduced. In Section 3, an accurate analytical model of the REMC-NFM is established by using the equivalent magnetic circuit method with consideration of magnetic leakage effect, edge effect and permeability

nonlinearity. Then the model is properly simplified in order to obtain the optimal pitch angle. In Section 4, FEM simulation is used to study the influence of crucial parameters on the performance of REMC-NFM. In Section 5, a prototype of the REMC-NFM is designed and manufactured, and a special experimental platform is built to measure its torque-angle and torque-displacement characteristics, and also magnetic flux density in the air gaps. The experimental results are then compared with both analytical results and FEM simulation. In Section 6, experimental results of conventional torque motor are compared with counterparts of REMC-NFM in order to validate the simplified model. Finally, some conclusions of this work are drawn in Section 7.

2 Structure and Working Principle

Figure 1 shows the structure of REMC-NFM which is composed of left and right yokes, left and right control coils, upper and lower permanent magnets (PM) and armature. Both the yoke and the armature are made of soft magnetic material DT4. The upper and lower PMs are respectively installed in the grooves of the left and right yokes, the control coils are respectively wound on the outer sides of the left and right yokes, and the armature is located in the middle of the REMC-NFM. The two sides of the armature are designed as inclined wing surfaces, which are centrally symmetrical about the rotating shaft. The angle between the wing surface of armature and the axial direction is defined as the pitch angle β , which is also the same as the angle of pole shoe surface of the yoke. When assembled, the armature inclined wing surface and the pole shoe surface of the yoke are parallel to each other, which forms four working air gaps with the same height.

The magnetic circuit diagram of REMC-NFM is shown in Figure 2. When the coil is not energized, the armature is in the middle position. All the air gap heights are equal to g and the REMC-NFM has no output torque. When the coil is energized in the direction shown in the Figure 2, the polarized magnetic flux ϕ_g (blue line) generated by the PMs and the control magnetic flux ϕ_c (red line) generated by the control coils are superimposed on each other in the four working air gaps. The magnetic flux at the air gap g_1 and g_3 is enhanced, and the magnetic flux at the air gap g_2 and g_4 is weakened. Therefore, an output torque is generated to drive

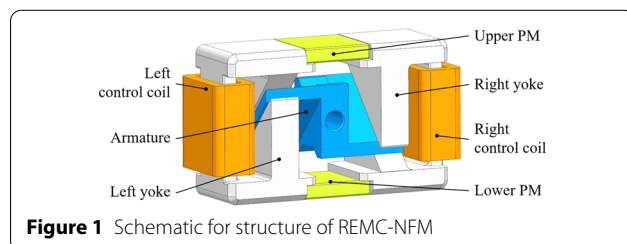


Figure 1 Schematic for structure of REMC-NFM

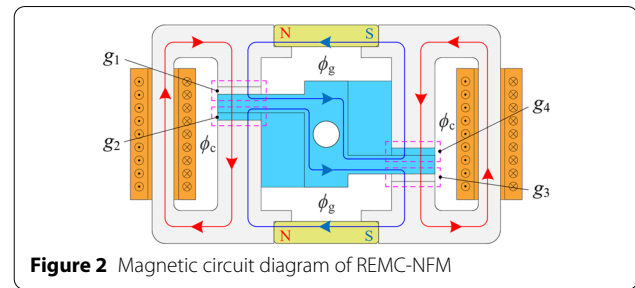


Figure 2 Magnetic circuit diagram of REMC-NFM

the armature to rotate. Besides, REMC-NFM also has a special negative feedback mechanism, which can be clarified by force analysis in Figure 3. When the armature rotates by the angle θ , the air gap height changes, therefore the output force F , its circumferential component force F_d and axial component force F_z all increase. And F_d generates a driving torque T_d to drive the armature to rotate. At this time, if an external force F_e such as hydraulic force exists to pull the armature to move with an axial displacement z according to the direction shown in Figure 3, the air gap height would be varied again and F will be reduced, which makes the armature to be acted by a torque T_r having the opposite direction with T_d . Thus, the armature will rotate in the opposite direction until it returns the initial position, so as to realize the negative feedback of force-displacement.

Figure 4 shows the novel 2D valve where REMC-NFM is used as EMC. There are small high-pressure hole and low-pressure hole machined on left spool land, which are connected to the oil supply and oil tank, respectively. There is a straight groove machined on internal surface of sleeve which is connected to sensitive chamber. The oil supply pressure P_s is led to high-pressure hole and high-pressure chamber through hole a and hole b. In the equilibrium position high-pressure hole and low-pressure hole are located on the two sides of straight groove and constitute two tiny overlapping openings, which forms a half-hydraulic resistance bridge. The output pressure of resistance bridge is then ported to the sensitive chamber. Neglecting Bernoulli's force and friction force and set the area of sensitive chamber as twice as that of high-pressure

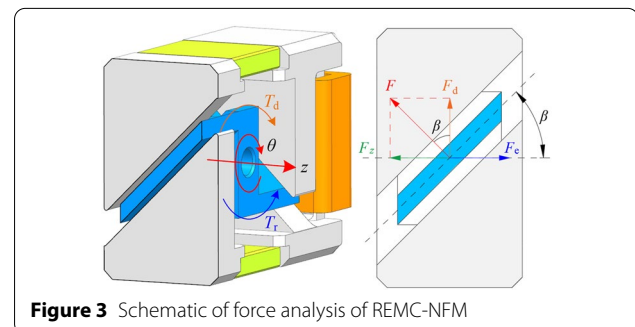
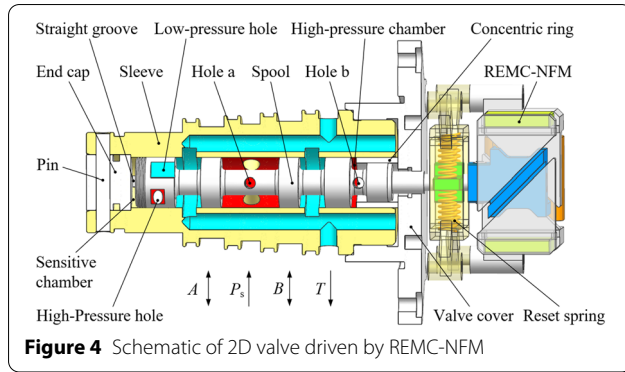


Figure 3 Schematic of force analysis of REMC-NFM



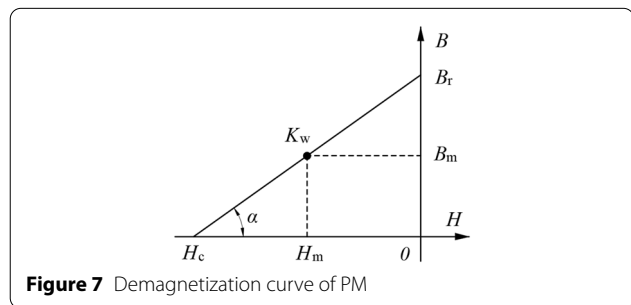
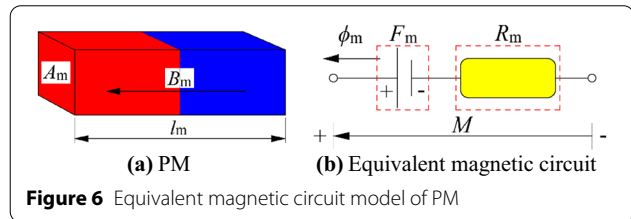
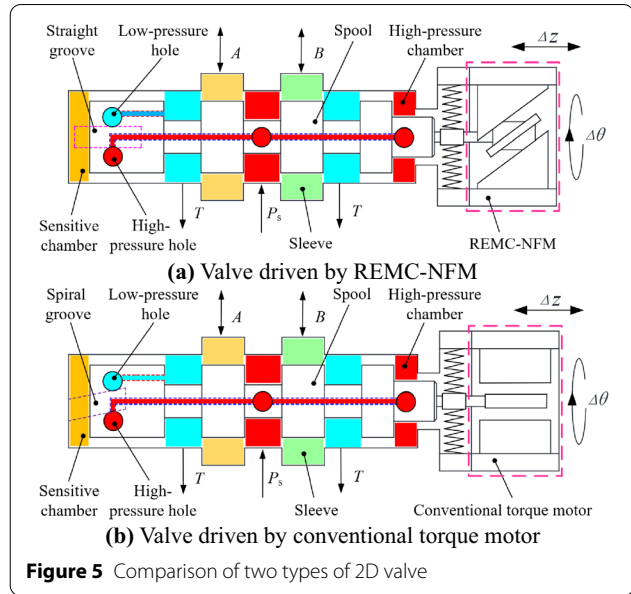
chamber, the spool can be in a hydrostatic force balance. When REMC-NFM is electrified, the spool also rotates with the armature, and this rotary motion varies the two overlapping openings differentially, which leads to the variation of sensitive chamber pressure. Then the hydrostatic force acting across the spool loses balance and spool begins to move axially. Due to this axial external force (F_e in Figure 3) and the slope design of armature, the working air gaps also varies with spool axial movement, which results in an additional negative feedback torque (T_r in Figure 3) to drive armature and spool rotate reversely until the working air gaps return to initial value and the overlap area of high-pressure hole and low-pressure hole also return to the state symmetrical to the straight groove, which re-establish the spool force balance. In essence, such design scheme has a force-displacement feedback characteristic. For comparison, Figure 5(b) gives schematic of 2D valve driven by conventional torque motor. It can be seen in Figure 5(a) that with proposed REMC-NFM, the spiral groove can be replaced by a straight groove.

3 Analytical Modelling

3.1 PM Modelling

Figure 6 shows the equivalent magnetic circuit model of the PM, which has a magnetization direction sectional area of A_m and a magnetization direction length of l_m . Figure 7 illustrates the demagnetization curve of PM, where K_w is the working point of the PM, α is the angle between the demagnetization curve and the H -axis, B_r is the residual magnetic flux density, H_c is the coercive force. The working coercive force H_m and the working magnetic flux density B_m corresponding to the K_w will vary with the variation of the working state.

When the working point K_w is on the demagnetization curve, the slope of the demagnetization curve represents the permeability μ_m , which can be written as:



$$\mu_m = \tan \alpha = -\frac{B_r}{H_c} = \frac{B_r - B_m}{-H_m} \quad (1)$$

The relationship between the working coercive force H_m and working magnetic flux density B_m corresponding to the K_w can be written as:

$$B_m = -\frac{B_r}{H_c}(H_m - H_c) = \mu_m(H_m - H_c) \quad (2)$$

The relationship between B_m and the magnetic flux generated by the PM ϕ_m can be written as:

$$B_m = \frac{\phi_m}{A_m} \quad (3)$$

Therefore, the relationship between H_m and B_m can be rewritten as:

$$H_m = \frac{\phi_m}{\mu_m A_m} + H_c. \quad (4)$$

After multiplying the length of magnetization direction l_m on both sides, we can get:

$$H_m l_m = \frac{\phi_m l_m}{\mu_m A_m} + H_c l_m, \quad (5)$$

where M is the magnetic potential generated by the PM; F_m is the magnetic potential provided to the external magnetic circuit; R_m is the internal magnetic reluctance of the permanent magnet. They can be calculated by the following formula:

$$\begin{cases} M = -H_c l_m, \\ F_m = -H_m l_m, \\ R_m = \frac{l_m}{\mu_m A_m}. \end{cases} \quad (6)$$

Therefore, Eq. (5) can be rewritten as:

$$-H_m l_m = -R_m \phi_m - H_c l_m, \quad (7)$$

$$M = F_m - R_m \phi_m. \quad (8)$$

Equation (8) demonstrates that the magnetic potential of PM is divided into two parts: One is the magnetic potential of the external magnetic circuit; The other is the internal magnetic potential drop of the PM.

3.2 Air Gap Reluctance Modelling

Since the permeability of air is much smaller than that of soft magnetic materials, the change of air gap reluctance will have a huge impact on the entire magnetic circuit. In order to obtain an accurate analytical model, an accurate air gap reluctance model is essential. When the magnetic flux flows through the air gap, a diffusion phenomenon occurs. A part of the magnetic flux flows through the edge of the magnetic pole face along other path, which can be called as the edge effect. Although this part of the magnetic flux is not huge, it still produces a non-negligible error, which shall be considered into the model. As shown in Figure 8, the path of the magnetic flux flowing through the air gap can be divided into several different magnetic flux tubes for calculation.

The air gap reluctance considering the edge effect is calculated by the magnetic field division method [34], where

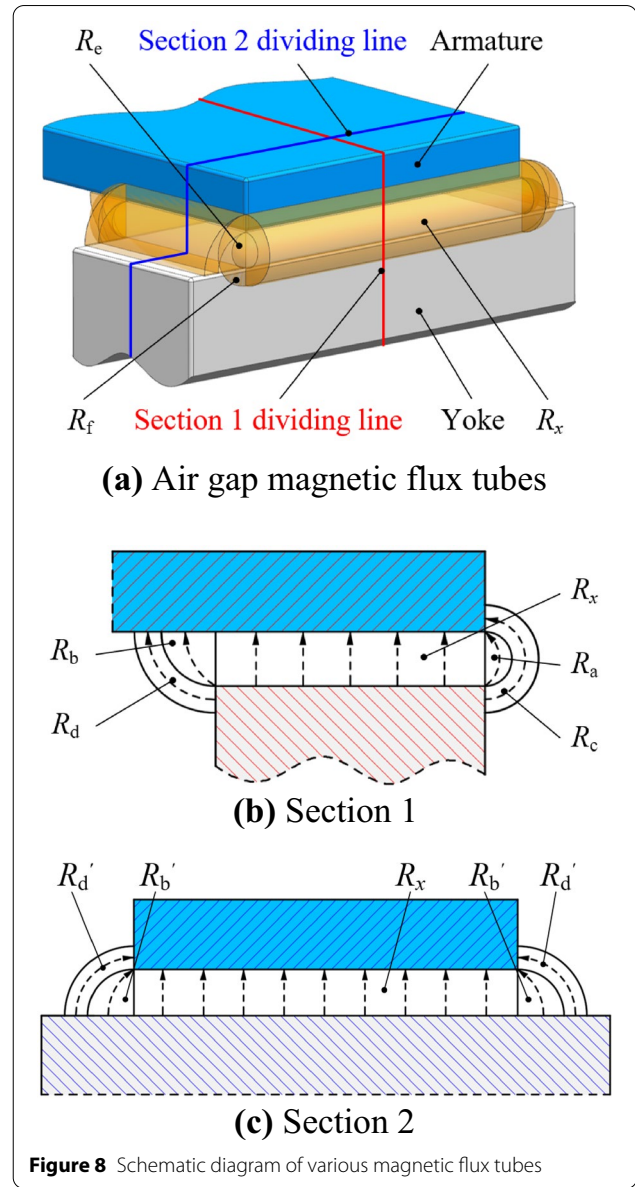


Figure 8 Schematic diagram of various magnetic flux tubes

the corresponding magnetic flux tube reluctance formula is shown in Table 1.

The magnetic reluctance calculation result of each magnetic flux tube is shown in Table 2.

For the scattered magnetic field of free space, $m = (1 \sim 2)n$, here $m = 1.1n$, L_{g1} is the air gap length, L_{g2} is the air gap width, therefore the working air gap reluctance R_{xg} considering the edge effect is obtained as:

$$R_{xg1} = R_{xg3} = \frac{1}{\frac{1}{R_{x1}} + \frac{1}{R_{a1}} + \frac{1}{R_{b1}} + \frac{2}{R_{b1}} + \frac{1}{R_{c1}} + \frac{1}{R_{d1}} + \frac{2}{R_{d1}} + \frac{4}{R_{e1}} + \frac{4}{R_{f1}}}, \quad (9)$$

Table 1 Reluctance calculation of various magnetic flux tubes

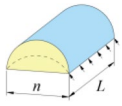
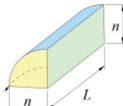

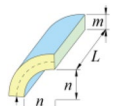
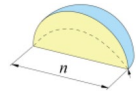
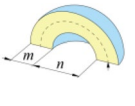
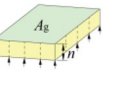
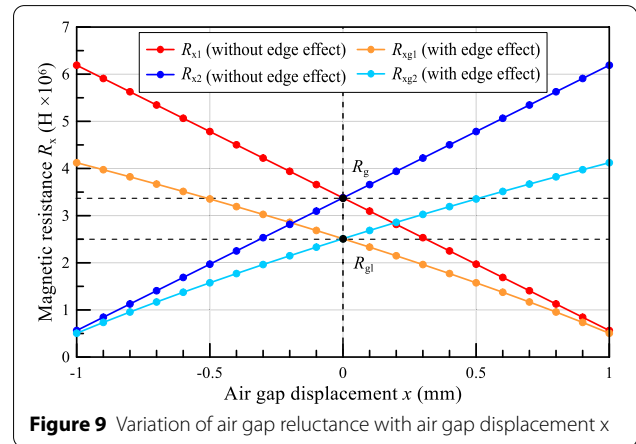
Number	1	2	3	4	5	6	7
Shapes of magnetic flux tubes							
Formula	$R = \frac{3.846}{\mu_0 L}$	$R = \frac{1.923}{\mu_0 L}$	$R = \frac{\pi}{\mu_0 L \ln(1 + \frac{2m}{n})}$	$R = \frac{\pi}{2\mu_0 L \ln(1 + \frac{m}{n})}$	$R = \frac{12.987}{\mu_0 n}$	$R = \frac{4}{\mu_0 m}$	$R = \frac{n}{\mu_0 A_g}$

Table 2 Reluctance calculation result

Reluctance	Result
R_a	$R_{a1} = R_{a2} = \frac{3.846}{\mu_0 L_{g1}}$
R_b	$R_{b1} = R_{b2} = \frac{1.923}{\mu_0 L_{g1}}$
R'_b	$R'_{b1} = R'_{b2} = \frac{1.923}{\mu_0 L_{g2}}$
R_c	$R_{c1} = \frac{\pi}{\mu_0 L_{g1} \ln(1 + \frac{2m}{g-x})}$ $R_{c2} = \frac{\pi}{\mu_0 L_{g1} \ln(1 + \frac{2m}{g+x})}$
R_d	$R_{d1} = \frac{\pi}{2\mu_0 L_{g1} \ln(1 + \frac{m}{g-x})}$ $R_{d2} = \frac{\pi}{2\mu_0 L_{g1} \ln(1 + \frac{m}{g+x})}$
R'_d	$R'_{d1} = \frac{\pi}{2\mu_0 L_{g2} \ln(1 + \frac{m}{g-x})}$ $R'_{d2} = \frac{\pi}{2\mu_0 L_{g2} \ln(1 + \frac{m}{g+x})}$
R_e	$R_{e1} = \frac{12.987}{\mu_0 (g-x)}, R_{e2} = \frac{12.987}{\mu_0 (g+x)}$
R_f	$R_{f1} = R_{f2} = \frac{4}{\mu_0 m}$
R_x	$R_{x1} = \frac{g-x}{\mu_0 A_g}, R_{x2} = \frac{g+x}{\mu_0 A_g}$

**Figure 9** Variation of air gap reluctance with air gap displacement x

and ϕ_{L2} generated by the PMs and the control coils is difficult to be calculated, we unify the paths of the leakage flux and connect them in parallel with the PMs and the control coils in magnetic circuit, as shown in Figure 10. Therefore, ϕ_{L1} and ϕ_{L2} can be expressed as:

$$R_{xg2} = R_{xg4} = \frac{1}{\frac{1}{R_{x2}} + \frac{1}{R_{a2}} + \frac{1}{R_{b2}} + \frac{2}{R_{b2}} + \frac{1}{R_{c2}} + \frac{1}{R_{d2}} + \frac{2}{R'_{d2}} + \frac{4}{R_{e2}} + \frac{4}{R_{f2}}}. \quad (10)$$

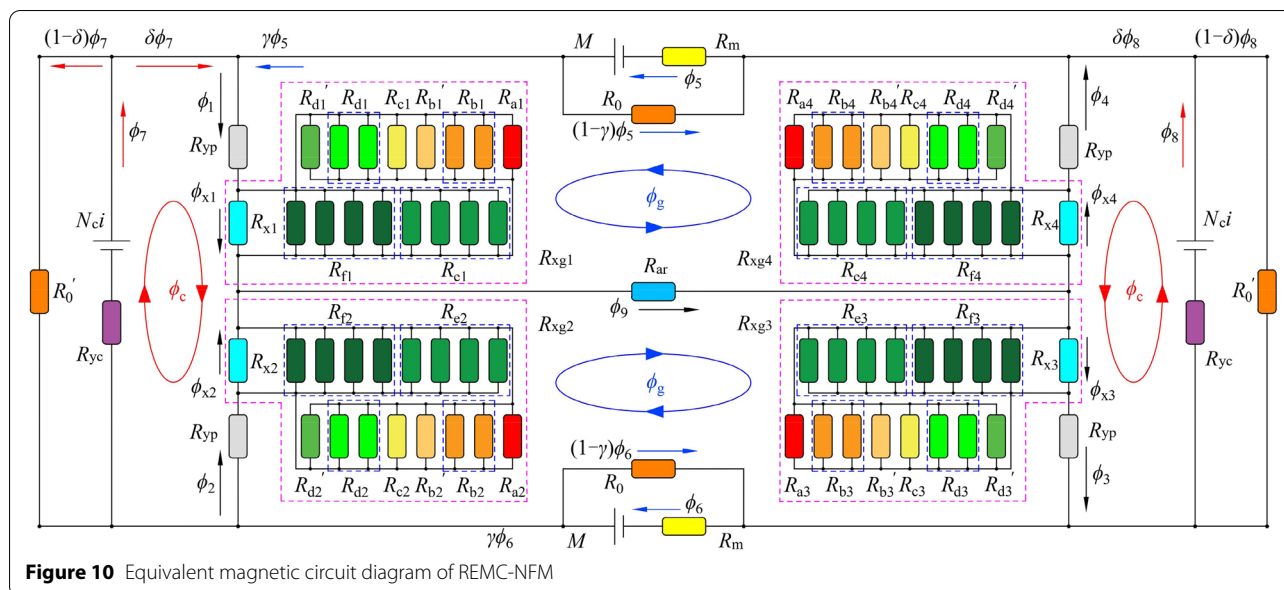
Figure 9 shows the calculated variation of air gap reluctance with air gap displacement x both under the situation with and without edge effect. It can be clearly seen that R_{xg1} and R_{xg2} are both smaller than R_{x1} and R_{x2} , which proves the necessity of considering the edge effect in order to have an accurate analytical model.

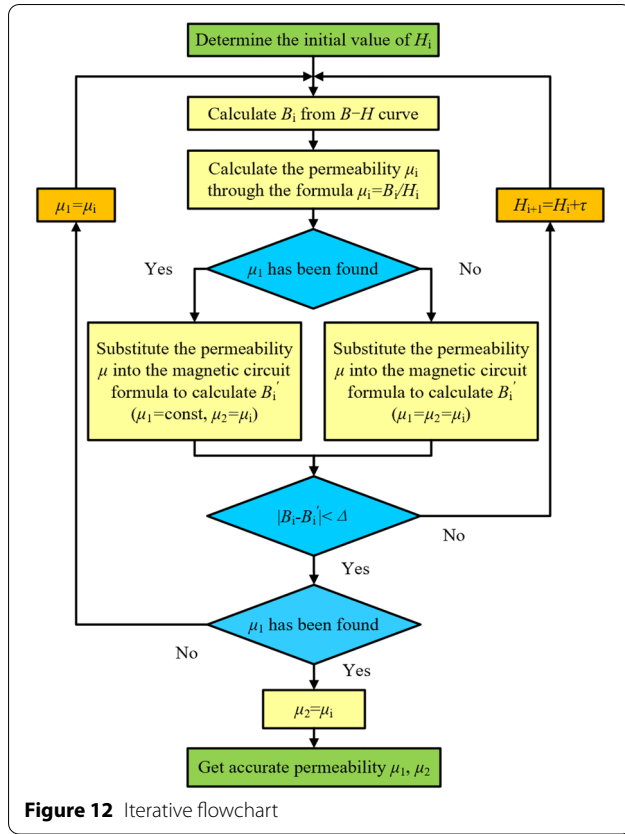
3.3 Equivalent Magnetic Circuit Modeling

For the traditional equivalent magnetic circuit modelling, the leakage flux generated by the PMs and the control coils is usually ignored. In order to improve the accuracy of the analytical model of REMC-NFM, magnetic leakage effect needs to be considered. Since the leakage flux ϕ_{L1}

$$\begin{cases} \phi_{L1} = (1 - \gamma)\phi_5, \\ \phi_{L2} = (1 - \delta)\phi_7, \end{cases} \quad (11)$$

where γ represents the flux utilization of PM, and δ represents the flux utilization of control coil. Finally, the whole equivalent magnetic circuit diagram of the REMC-NFM is shown in Figure 10. The black solid line represents the magnetic circuit, the rounded rectangle represents the magnetic reluctance, and the arrow represents the direction of the magnetic flux. The purple dashed box contains all the air gap magnetic reluctance considering the edge effect, and the blue dashed box contains the same type of magnetic flux tubes.





accuracy and τ is the iteration step size. Since the B and H of the armature and the yoke are different, the permeability is also different, it is necessary to repeatedly iterate to obtain the accurate values of the permeability of the armature and the yoke.

3.5 Torque Calculation

Combining Eqs. (12)–(15), the detailed expressions of the total magnetic flux ϕ_1 on the strengthening side and the total magnetic flux ϕ_2 on the weakening side of the working air gaps can be written as:

$$\begin{aligned} \phi_1 = \phi_3 = & (MR_{yc}\gamma + R_m\delta N_c i + 2MR_2\gamma\delta + 2R_2\gamma\delta N_c i \\ & + 2R_{ar}\gamma\delta N_c i)/(R_{yc}R_m + R_1R_m\delta + R_2R_m\delta \\ & + R_1R_{yc}\gamma + R_2R_{yc}\gamma + 2R_{yc}R_{ar}\gamma + 4R_1R_2\gamma\delta \\ & + 2R_1R_{ar}\gamma\delta + 2R_2R_{ar}\gamma\delta), \end{aligned} \quad (17)$$

$$\begin{aligned} \phi_2 = \phi_4 = & -(R_m\delta N_c i - MR_{yc}\gamma - 2MR_1\gamma\delta + 2R_1\gamma\delta N_c i \\ & + 2R_{ar}\gamma\delta N_c i)/(R_{yc}R_m + R_1R_m\delta + R_2R_m\delta \\ & + R_1R_{yc}\gamma + R_2R_{yc}\gamma + 2R_{yc}R_{ar}\gamma + 4R_1R_2\gamma\delta \\ & + 2R_1R_{ar}\gamma\delta + 2R_2R_{ar}\gamma\delta). \end{aligned} \quad (18)$$

Through calculation, the main flux ϕ_{x1} on the strengthening side and the main flux ϕ_{x2} on the weakening side of the working air gaps can be written as:

$$\begin{aligned} \phi_{x1} = \phi_1 \frac{1}{R_{x1}} / & \left(\frac{1}{R_{x1}} + \frac{1}{R_{a1}} + \frac{1}{R_{b1}} \right. \\ & + \frac{2}{R'_{b1}} + \frac{1}{R_{c1}} + \frac{1}{R_{d1}} + \frac{2}{R'_{d1}} \\ & \left. + \frac{4}{R_{e1}} + \frac{4}{R_{f1}} \right), \end{aligned} \quad (19)$$

$$\begin{aligned} \phi_{x2} = \phi_2 \frac{1}{R_{x2}} / & \left(\frac{1}{R_{x2}} + \frac{1}{R_{a2}} + \frac{1}{R_{b2}} + \frac{2}{R'_{b2}} \right. \\ & + \frac{1}{R_{c2}} + \frac{1}{R_{d2}} + \frac{2}{R'_{d1}} + \frac{4}{R_{e1}} + \frac{4}{R_{f1}} \left. \right). \end{aligned} \quad (20)$$

Thus, the magnetic flux density B_1 on the strengthening side and the magnetic flux density B_2 on the weakening side of the working air gaps can be obtained:

$$\begin{cases} B_1 = B_3 = \frac{\phi_{x1}}{A_g}, \\ B_2 = B_4 = \frac{\phi_{x2}}{A_g}. \end{cases} \quad (21)$$

According to Maxwell's electromagnetic force formula, the single-side output force can be obtained:

$$F = \frac{1}{2} \left| \frac{d}{dx} \frac{U^2}{R} \right| = \frac{1}{2} \left| \frac{d}{dx} \left[\frac{\phi(g+x)^2}{\mu_0 A_g} \left(\frac{\mu_0 A_g}{g+x} \right) \right] \right| = \frac{\phi^2}{2\mu_0 A_g}, \quad (22)$$

$$\begin{cases} F_1 = \frac{\phi_{x1}^2}{2\mu_0 A_g}, \\ F_2 = \frac{\phi_{x2}^2}{2\mu_0 A_g}, \end{cases} \quad (23)$$

where F_1 and F_2 are the electromagnetic output force on the magnetic flux strengthening side and weakening side, respectively. Multiplying with the force arm a , the resulting torque T can be obtained:

$$T = 2a(F_1 - F_2)\cos\beta = \frac{a}{\mu_0 A_g} (\phi_{x1}^2 - \phi_{x2}^2)\cos\beta. \quad (24)$$

Substituting Eqs. (6), (9), (10), (12)–(15), (17)–(20) into Eqs. (21)–(24), the precise formulas of magnetic flux density and torque can be obtained. For simplification, these formulas are attached and referred as Eqs. (48)–(50) in the Appendix, which will be used for analytical calculation.

3.6 Model Simplification

The above-discussed analytical model has advantages of rapid and accurate calculation in the pre-design stage. However, it is too complicated to be used for qualitative analysis. In order to perform qualitative analysis and find optimal pitch angle. The above-discussed analytical model is further simplified in this part. Referring to Figure 9, the curves of variation of magnetic reluctance can be fitted to linear lines, which can be written as:

$$\begin{cases} R_{x1} = (1 - kx)R_{gl}, \\ R_{x2} = (1 + kx)R_{gl}, \\ k = \left. \frac{dR_{xg}}{dx} \right|_{x=0}, \\ R_{gl} = R_{xg}|_{x=0}. \end{cases} \quad (25)$$

The polarized magnetic flux ϕ_g generated by the PMs and the control magnetic flux ϕ_c generated by the control coils are respectively written as:

$$\phi_g = \frac{\gamma M}{2\gamma R_{yp} + 2\gamma R_{gl} + R_m + \gamma R_{ar}}, \quad (26)$$

$$\phi_c = \frac{\delta N_c i}{2\delta R_{gl} + 2\delta R_{yp} + R_{yc}}. \quad (27)$$

From Eq. (12), we can have:

$$\begin{cases} \phi_5 = \phi_6 = \frac{\phi_1 + \phi_2}{2\gamma}, \\ \phi_9 = \phi_1 + \phi_2, \\ \phi_7 = \phi_8 = \frac{\phi_1 - \phi_2}{2\delta}. \end{cases} \quad (28)$$

Substituting Eq. (28) into Eq. (13), we can get:

$$\begin{aligned} M = & \phi_1 \left[R_{yp} + (1 - kx)R_{gl} + \frac{R_m}{2\gamma} + R_{ar} \right] \\ & + \phi_2 \left[R_{yp} + (1 + kx)R_{gl} + \frac{R_m}{2\gamma} + R_{ar} \right], \end{aligned} \quad (29)$$

$$\begin{aligned} N_c i = & \phi_1 \left[R_{yp} + (1 - kx)R_{gl} + \frac{R_{yc}}{2\delta} \right] \\ & - \phi_2 \left[R_{yp} + (1 + kx)R_{gl} + \frac{R_{yc}}{2\delta} \right]. \end{aligned} \quad (30)$$

Substitute Eqs. (26) and (27) into the above formulas, we can have:

$$\begin{aligned} \phi_g \left(2R_{yp} + 2R_{gl} + \frac{R_m}{\gamma} + R_{ar} \right) \\ = \phi_1 \left[R_{yp} + (1 - kx)R_{gl} + \frac{R_m}{2\gamma} + R_{ar} \right] \\ + \phi_2 \left[R_{yp} + (1 + kx)R_{gl} + \frac{R_m}{2\gamma} + R_{ar} \right], \end{aligned} \quad (31)$$

$$\begin{aligned} \phi_c \left(2R_{gl} + 2R_{yp} + \frac{R_{yc}}{\delta} \right) \\ = \phi_1 \left[R_{yp} + (1 - kx)R_{gl} + \frac{R_{yc}}{2\delta} \right] \\ - \phi_2 \left[R_{yp} + (1 + kx)R_{gl} + \frac{R_{yc}}{2\delta} \right]. \end{aligned} \quad (32)$$

Based on Eqs. (31) and (32), the total magnetic flux ϕ_1 and ϕ_2 of the working air gaps can be rewritten as:

$$\begin{aligned} \phi_2 = \phi_4 = & \frac{t}{t - k^2 x^2} \left[\left(1 - \frac{2kx\delta R_{gl}}{2\delta R_{gl} + 2\delta R_{yp} + R_{yc}} \right) \phi_g \right. \\ & \left. + \left(\frac{2kx\gamma R_{gl}}{2\gamma R_{yp} + 2\gamma R_{gl} + R_m + \gamma R_{ar}} - 1 \right) \phi_c \right], \end{aligned} \quad (33)$$

$$\begin{aligned} \phi_1 = \phi_3 = & \frac{t}{t - k^2 x^2} \left[\left(1 + \frac{2kx\delta R_{gl}}{2\delta R_{gl} + 2\delta R_{yp} + R_{yc}} \right) \phi_g \right. \\ & \left. + \left(1 + \frac{2kx\gamma R_{gl}}{2\gamma R_{yp} + 2\gamma R_{gl} + R_m + \gamma R_{ar}} \right) \phi_c \right], \end{aligned} \quad (34)$$

where

$$t = \frac{(2\gamma R_{yp} + 2\gamma R_{gl} + R_m + \gamma R_{ar})(2\delta R_{gl} + 2\delta R_{yp} + R_{yc})}{4\gamma\delta R_{gl}^2}. \quad (35)$$

The main magnetic flux ϕ_{x1} and ϕ_{x2} can be expressed as:

$$\begin{cases} \phi_{x1} = \frac{R_g}{R_{gl}} \phi_1, \\ \phi_{x2} = \frac{R_g}{R_{gl}} \phi_2. \end{cases} \quad (36)$$

R_g represents the main air gap magnetic reluctance at the initial position, and R_{gl} represents the entire air gap

magnetic reluctance considering the edge effect at the initial position. Also we can have:

$$\phi_1 + \phi_2 = \left(2\phi_g + \frac{4kx\gamma R_{gl}}{2\gamma R_{yp} + 2\gamma R_{gl} + R_m + \gamma R_{ar}} \phi_c \right) \frac{R_g}{R_{gl}} \frac{t}{t - k^2 x^2}, \quad (37)$$

$$\phi_1 - \phi_2 = \left(\frac{4kx\delta R_{gl}}{2\delta R_{gl} + 2\delta R_{yp} + R_{yc}} \phi_g + 2\phi_c \right) \frac{R_g}{R_{gl}} \frac{t}{t - k^2 x^2}. \quad (38)$$

Substituting the above formulas into Eq. (23), we can have:

$$\begin{aligned} T = & \frac{a}{\mu_0 A_g} \left(2\phi_g + \frac{4kx\gamma R_{gl}}{2\gamma R_{yp} + 2\gamma R_{gl} + R_m + \gamma R_{ar}} \phi_c \right) \\ & \times \left(\frac{4kx\delta R_{gl}}{2\delta R_{gl} + 2\delta R_{yp} + R_{yc}} \phi_g + 2\phi_c \right) \\ & \times \left(\frac{t}{t - k^2 x^2} \frac{R_g}{R_{gl}} \right)^2 \cos\beta. \end{aligned} \quad (39)$$

For actual situation, the REMC-NFM's working angle can be very small, and when the angle is extremely small, $\sin\theta = \Delta x/a = \theta$, therefore, $\Delta x = a\theta$. And because the air gap height in the model is calculated perpendicular to the air gap magnetic pole surface, it is necessary to convert the rotation angle θ and axial displacement z into a displacement perpendicular to the air gap surface. Thus, the air gap displacement x can be written as

$$x = a\theta\cos\beta - z\sin\beta. \quad (40)$$

Substituting Eq. (40) into Eq. (39), it yields:

$$\begin{aligned} T = & \left(\frac{t}{t - k^2 x^2} \frac{R_g}{R_{gl}} \right)^2 \cos\beta [2ka\phi_g \\ & N_c \xi \left(1 + \xi^2 \eta k^2 x^2 \right) i \\ & + 4R_g k \frac{a^2}{g} \phi_g^2 \xi \left(1 + \eta \frac{\phi_c^2}{\phi_g^2} \right) \theta \cos\beta \\ & - 4R_g k \frac{a}{g} \phi_g^2 \xi \left(1 + \eta \frac{\phi_c^2}{\phi_g^2} \right) z \sin\beta], \end{aligned} \quad (41)$$

where

$$\begin{cases} \xi = \frac{2R_g \phi_c}{N_c i}, \\ \eta = \frac{N_c i \phi_g}{\phi_c M}. \end{cases} \quad (42)$$

Since the air gap displacement x is much smaller than the air gap height g , $k^2 x^2 \ll 1$. Thus, Eq. (41) can be further simplified as:

$$\begin{aligned} T = & \left(\frac{R_g}{R_{gl}} \right)^2 \cos\beta (2ka\phi_g N_c \xi i \\ & + 4R_g k \frac{a^2}{g} \phi_g^2 \xi \cos\beta \theta \\ & - 4R_g k \frac{a}{g} \phi_g^2 \xi \sin\beta z). \end{aligned} \quad (43)$$

Equation (40) can be rewritten as:

$$T = K_t i + K_{mr} \theta - K_{ml} z, \quad (44)$$

where K_t is defined as electromagnetic torque coefficient; K_{mr} is defined as rotary magnetic spring stiffness; K_{ml} is defined as linear magnetic spring stiffness. K_t , K_{mr} and K_{ml} can be expressed as

$$\begin{cases} K_t = 2ka\phi_g N_c \xi \left(\frac{R_g}{R_{gl}} \right)^2 \cos\beta, \\ K_{mr} = 4R_g k \frac{a^2}{g} \phi_g^2 \xi \left(\frac{R_g}{R_{gl}} \right)^2 \cos^2\beta, \\ K_{ml} = 2R_g k \frac{a}{g} \phi_g^2 \xi \left(\frac{R_g}{R_{gl}} \right)^2 \sin 2\beta. \end{cases} \quad (45)$$

Equation (44) clearly illustrates that the torque equation of REMC-NFM contains three terms, where the first term $K_t i$ is the electromagnetic torque produced by

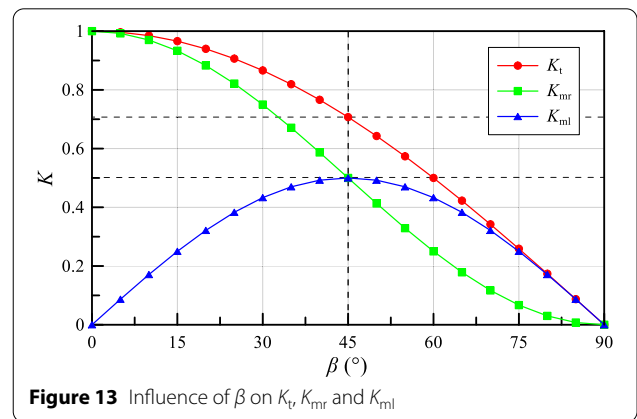


Figure 13 Influence of β on K_t , K_{mr} and K_{ml}

the control current when the armature is in the neutral position; the second term $K_{mr}\theta$ is the additional electromagnetic torque generated by the armature rotation; the last term $K_{ml}z$ is the additional electromagnetic torque generated by the armature linear displacement. Finally, it should be noted that the minus sign before the last $K_{ml}z$ indicates that the direction of driving torque and feedback torque shall be opposite.

3.7 Optimal Pitch Angle β

The design of REMC-NFM needs to take both driving and feedback performance into account. Based on Eq. (45), the influence of β on K_t , K_{mr} and K_{ml} can be graphed, as shown in Figure 13. It can be found that β has different influence on these three coefficients. For K_t and K_{mr} , they keep decreasing with the increase of β . For K_{ml} , it increases firstly and then decreases with the increase of β . Both the term $\sin 2\beta$ of Eq. (45) and Figure 13 reveal that K_{ml} reaches the maximum value when β is 45° . Therefore, choosing β as 45° is the optimal solution in order to maximize the feedback performance.

4 FEM Simulation

4.1 Simulation Verification

In order to improve and verify the accuracy of the analytical model, a FEM model is established using Ansoft/Maxwell software. Figure 14 shows the magnetic flux line distribution of REMC-NFM on different sections. It can be seen that both the PMs and the control coils have

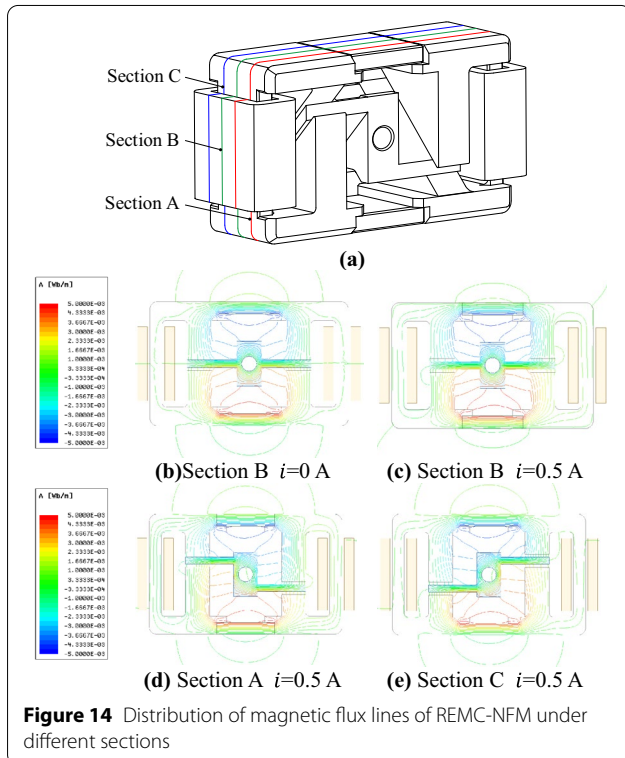


Figure 14 Distribution of magnetic flux lines of REMC-NFM under different sections

obvious magnetic leakage phenomenon, and there is a scattered magnetic flux at the working air gaps. This confirms the necessity of considering magnetic leakage effect and edge effects. Besides, in order to provide reference for determination of the PM flux utilization γ and control coils flux utilization δ , the magnetic flux lines generated by the PMs and the control coils passing through the air gaps are counted separately, and then compared with the total magnetic flux lines. For example, as shown in Figure 14(c), it can be measured that the ratio of the magnetic field lines of the PMs passing through the air gaps to the total number of the lines is 8:17, thus $\gamma=0.47$. By varying the current and the density of magnetic flux lines, more accurate coefficient values can be obtained, which will be given later on.

4.2 Parameters Optimization

Some crucial parameters have an important influence on the characteristics of REMC-NFM. In this part, three parameters, i.e., number of coil turn N_c , air gap height g and pitch angle β , are selected for simulation design optimization.

The analysis and simulation comparison curves of the influence of g on the torque are shown in Figure 15. The analytical results and FEM simulated results are very

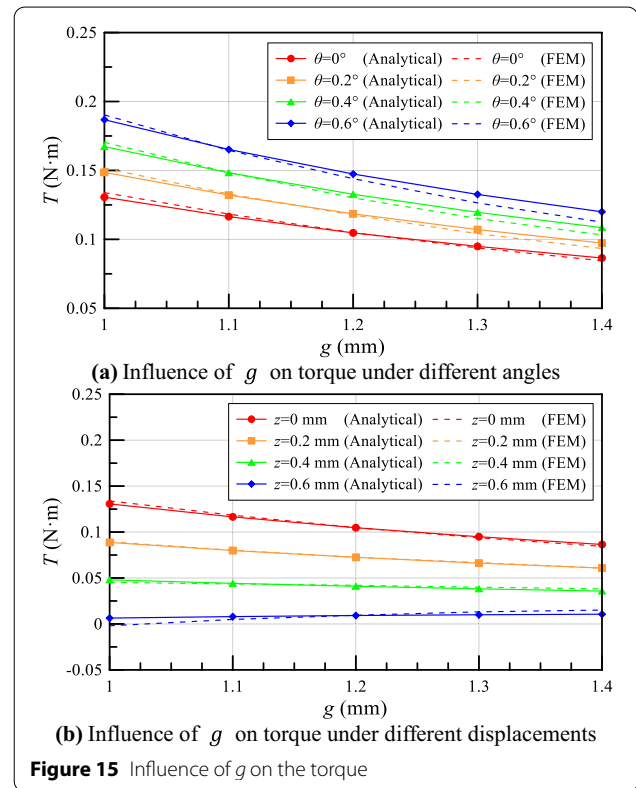
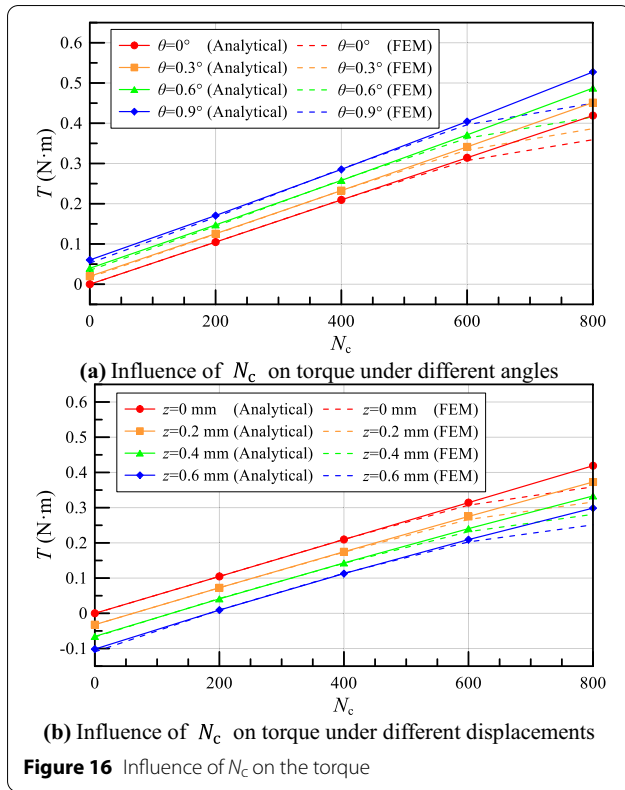


Figure 15 Influence of g on the torque



close. In Figure 15(a), the torque reaches 0.190, 0.165, 0.144, 0.126 and 0.112 N·m when the angle is 0.6° . In Figure 15(b), when the displacement is 0.6 mm, the torque reaches -0.002 , 0.005, 0.009, 0.013 and 0.015 N·m. Therefore, reducing g can improve both driving and feedback characteristics.

The analysis and simulation comparison curves of the influence of N_c are shown in Figure 16. In Figure 16(a), the torque reaches 0.053, 0.167, 0.287, 0.396 and 0.449 N·m when the angle is 0.9° . In Figure 16(b), when the displacement is 0.6 mm, the torque reaches -0.109 , 0.009, 0.114, 0.203 and 0.251 N·m. Therefore, increasing N_c can improve both driving and feedback characteristics. When N_c reaches above 600, the simulated value tends to be lower than the analytical value. This is because the excessive N_c cause magnetic saturation. Therefore, appropriate value of N_c should be selected.

The analysis and simulation comparison curves of the influence of the β on the torque are shown in Figure 17. As shown in Figure 17(a), increasing β will reduce the driving torque. When the rotation angle is 0.6° , the torque reaches 0.076, 0.071, 0.056, 0.035, 0.018, 0.004 and 0 N·m, respectively. As shown in Figure 17(b), the absolute value of torque first increases and then decreases, which reaches the maximum when β is 45° , and returns to 0 N·m when β is 90° . This result is consistent with the analytical analysis of Section 3.6, which further verifies the accuracy of the simplified model. When the displacement is 0.6 mm, the torque reaches

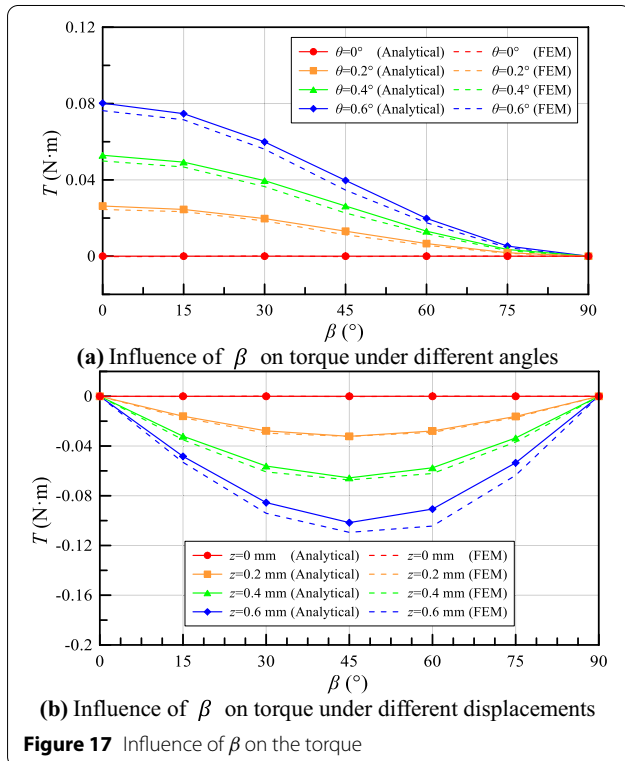


Table 3 Main design parameters for prototype of REMC-NFM

Parameter	Value
Coercive force H_c (A/m)	-890000
PM length l_m (mm)	24
PM permeability μ_m (H/m)	$1.0997 \times \mu_0$
PM sectional area A_m (mm ²)	5×18
Armature force arm length a (mm)	23.5
Armature length l_{ar} (mm)	50
Armature sectional area A_{ar} (mm ²)	3×28.3
Yoke pole shoe length l_{yp} (mm)	15
Yoke pole shoe sectional area A_{yp} (mm ²)	10×20
Yoke coil length l_{yc} (mm)	35
Yoke coil sectional area A_{yc} (mm ²)	5×18
Armature permeability μ_1 (H/m)	0.0048
Yoke permeability μ_2 (H/m)	0.0102
Air gap area A_g (mm ²)	10×28.3
Air gap length L_{g1} (mm)	28.3
Air gap width L_{g2} (mm)	10
PM flux utilization γ	0.45
Control coil flux utilization δ	0.85
Pitch angle β ($^\circ$)	45

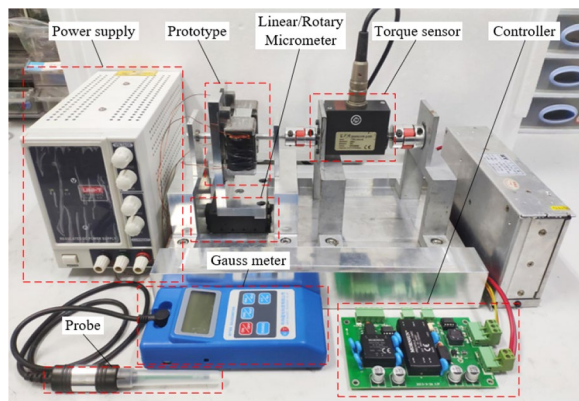


Figure 18 Experimental platform

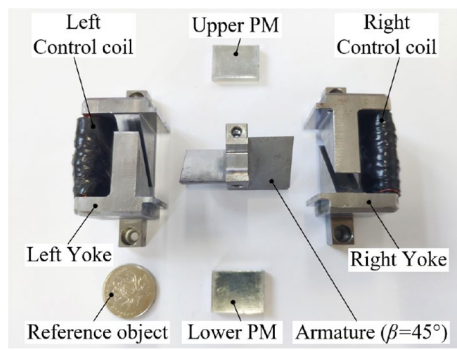


Figure 19 Experimental prototype of REMC-NFM

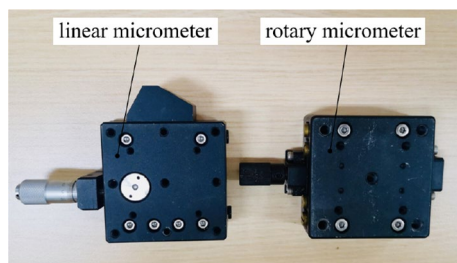
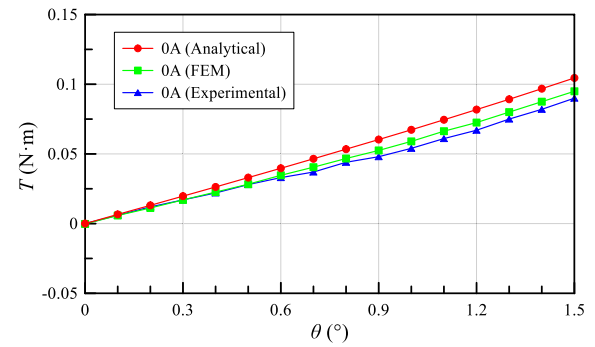
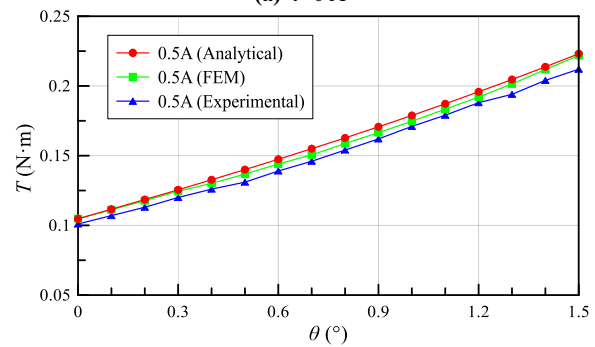


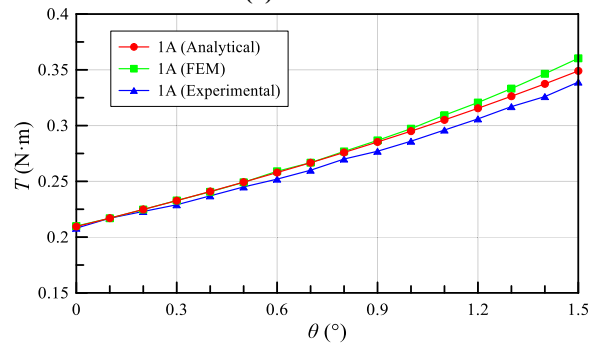
Figure 20 Linear micrometer and rotary micrometer



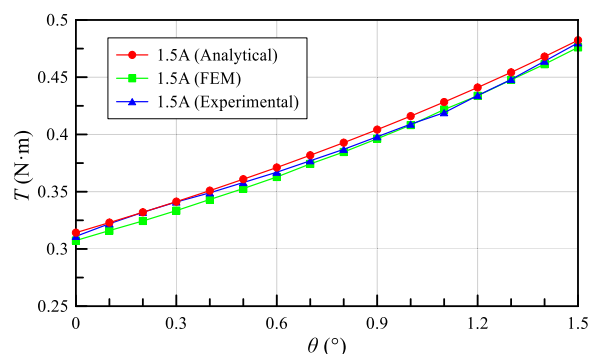
(a) $i=0$ A



(b) $i=0.5$ A



(c) $i=1$ A



(d) $i=1.5$ A

Figure 21 Torque-angle characteristics of REMC-NFM

Table 4 Comparison of torque-angle characteristics

i (A)		0	0.5	1	1.5
T (N·m) ($\theta = 1.5^\circ$)	Analytical	0.105	0.223	0.349	0.482
	FEM	0.095	0.222	0.360	0.476
	Experimental	0.090	0.212	0.339	0.480

0, -0.053 , -0.094 , -0.109 , -0.104 , -0.064 and 0 N·m, respectively. Finally, based on the analytical modelling and FEM optimization, the main design parameters for prototype of REMC-NFM can be determined, as listed in Table 3.

5 Experiment

In order to further verify the analytical model and FEM simulation results, prototype of REMC-NFM is manufactured and an experimental platform is built, as shown in Figures 18 and 19, respectively. The experimental platform mainly includes DC power supply, torque sensor, controller, Gauss meter, linear and rotary micrometer. In order to measure the torque-angle and torque-displacement characteristic curve of REMC-NFM, the linear and rotary micrometer are used and can be replaced with each other to vary the relative angle and displacement between the yoke and the armature, as shown in Figure 20. The armature is fixedly connected to the torque sensor through the shaft and coupling, and the yoke is fixedly connected to the rotary or linear micrometer through the fixed plate. The micrometer can be adjusted manually, so that the output torque of REMC-NFM at any position of armature can be measured. Change the current and repeat the experiment, the torque characteristic curve can be obtained. The Gauss meter is used to measure the magnetic flux density of the working air gap at the corresponding position.

5.1 Torque-Angle Characteristics

Torque-angle characteristics are measured when the current i is 0, 0.5, 1 and 1.5 A, respectively. The results are then compared with analytical and FEM simulated counterparts, as shown in Figure 21. Table 4 summarizes the results comparison. It can be seen that with the increase of current and rotation angle, the torque presents an increasing trend, which is consistent with the analysis of $K_t i$ and $K_{mr} \theta$ in Eq. (44). Besides, the analytical, FEM simulated and experimental results are in good agreement, which verifies the accuracy of analytical model of REMC-NFM. When $i=1.5$ A and $\theta=1.5^\circ$, the analytical,

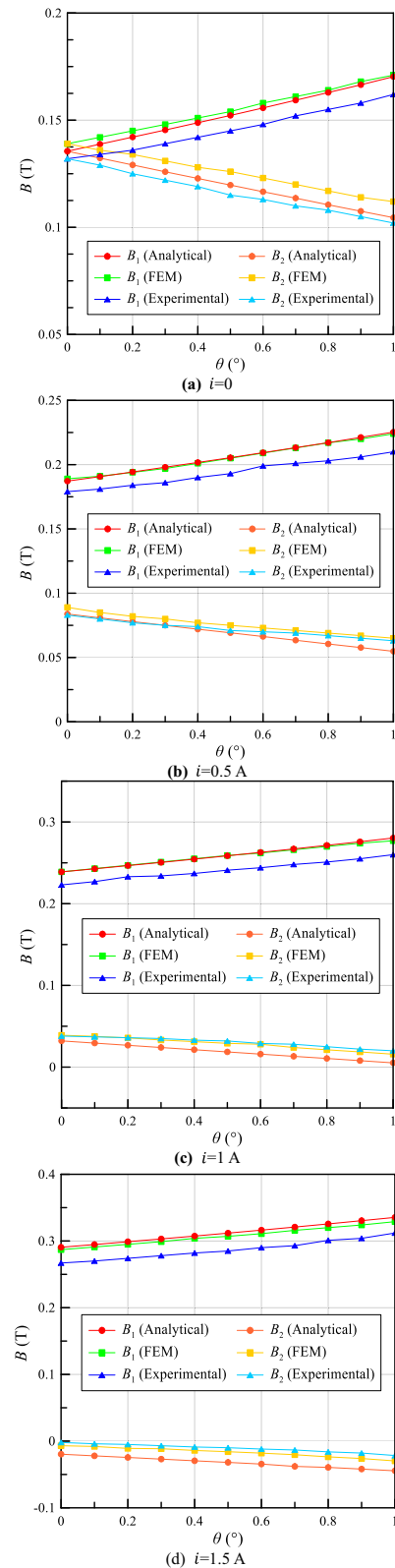
**Figure 22** Magnetic flux densities under different currents and rotation angles

Table 5 Comparison of magnetic flux densities under different currents and rotation angles

i (A)		0	0.5	1	1.5
B_1 (T) ($\theta = 1^\circ$)	Analytical	0.170	0.225	0.280	0.335
	FEM	0.171	0.224	0.277	0.329
	Experimental	0.162	0.210	0.260	0.312
B_2 (T) ($\theta = 1^\circ$)	FEM	0.112	0.065	0.016	-0.030
	Analytical	0.104	0.055	0.005	-0.045
	Experimental	0.102	0.063	0.020	-0.022

FEM simulated and experimental results are 0.482, 0.476, and 0.480 N·m, respectively.

Magnetic flux densities are also measured when the current i is 0, 0.5, 1 and 1.5 A, respectively. The results are then compared with analytical and FEM simulated counterparts, as shown in Figure 22. Table 5 summarizes the magnetic flux density B_1 on the strengthening side and the magnetic flux density B_2 on the weakening side. In the initial position, due to the symmetrical arrangement of the PMs, the same magnitude of magnetic flux exists in all air gaps without electricity. As the rotation angle increases, B_1 increases and B_2 decreases, and as the current increases, the difference between B_1 and B_2 gradually increase. When $i = 1.5$ A and $\theta = 1^\circ$, the analytical, FEM simulated and experimental results of B_1 are 0.335, 0.329 and 0.312 T, respectively. And the counterparts of B_2 are -0.030, -0.045 and -0.022 T, respectively. The differential variation of B again validates the working principle of REMC-NFM discussed previously. Besides, there is a difference between analytical and experimental results of B_2 , which is more obvious when the current increases. The reason for this may be lies in two aspects: one is the unpredictable measuring errors since the region of working air gap is quite small; The other is the possibility of uneven texture of DT4 materials.

5.2 Torque-Displacement Characteristics

In order to validate the feedback mechanism of REMC-NFM, the torque-displacement characteristics are measured by experiments when the current i is 0, 0.5, 1 and 1.5 A, respectively. The results are then compared with analytical and FEM simulated counterparts, as shown in Figure 23. Table 6 summarizes the results comparison. It can be seen that with the increase of armature displacement,

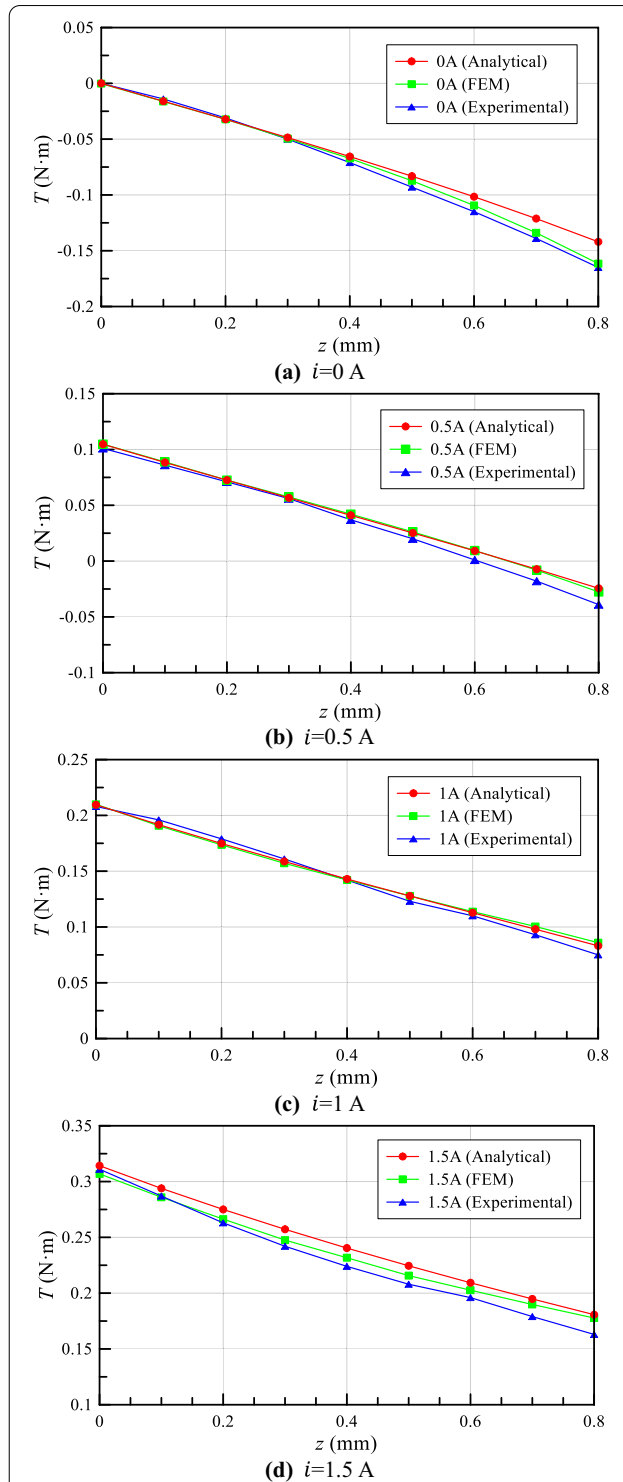
**Figure 23** Torque-displacement characteristics of REMC-NFM

Table 6 Comparison of torque-displacement characteristics

i (A)		0	0.5	1	1.5
T (N·m) ($z = 0.8$ mm)	Analytical	-0.142	-0.024	0.083	0.181
	FEM	-0.162	-0.028	0.086	0.178
	Experimental	-0.165	-0.039	0.075	0.163

the feedback torque increases. Note that here the measured torque is the sum of driving torque and feedback torque. Since the direction of driving torque and feedback torque is opposite, the measured overall torque is influenced by the increasing feedback torque and thus presents a downward trend, which is consistent with the analysis of $K_{ml}z$ in Eq. (44). When $i = 1.5$ A, $z = 0.8$ mm, the torque is 0.181, 0.178 and 0.163 N·m, respectively. Besides, the analytical, FEM simulated and experimental results are in good agreement, which verifies the accuracy of analytical model of REMC-NFM.

Magnetic flux density is measured again with the variation of current and armature displacement. The results are then compared with analytical and FEM simulated counterparts, as shown in Figure 24. Table 7 summarizes the magnetic flux density B_1 on the strengthening side and the magnetic flux density B_2 on the weakening side. Increase of displacement reduces B_1 and increases B_2 . When $i = 1.5$ A and $z = 0.6$ mm, the analytical, FEM simulated and experimental results of B_1 are 0.237, 0.235 and 0.216 T, respectively. And the counterparts of B_2 are 0.015, 0.021 and 0.024 T, respectively. Besides, the analytical, FEM simulated and experimental results are in good agreement, which also verifies the accuracy of analytical model of REMC-NFM.

6 Further Discussion

The idea of REMC-NFM was originated from the conventional torque motor, where the significant structure difference lies in the pitch angle β . For torque motor, $\beta = 0$, therefore it has no feedback ability and only has driving function. Eqs. (44) and (45) are also suitable for the torque motor, which can be written as:

$$T = K_t i + K_{mr} \theta, \quad (46)$$

$$\begin{cases} K_t = 2ka\phi_g N_c \xi \left(\frac{R_g}{R_{gl}} \right)^2, \\ K_{mr} = 4R_g k \frac{a^2}{g} \phi_g^2 \xi \left(\frac{R_g}{R_{gl}} \right)^2. \end{cases} \quad (47)$$

In order to validate the correctness of Eqs. (44) and (45) in Section 3.6, and also explore the relationship between the REMC-NFM and conventional torque motor, the prototype of torque motor which has the same dimensions as REMC-NFM is manufactured, as

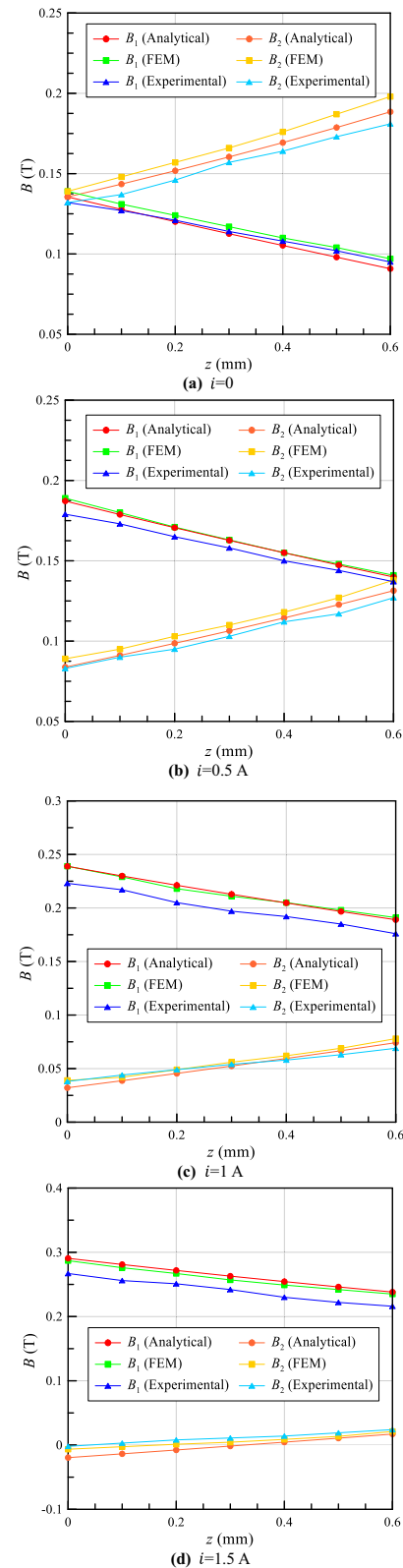
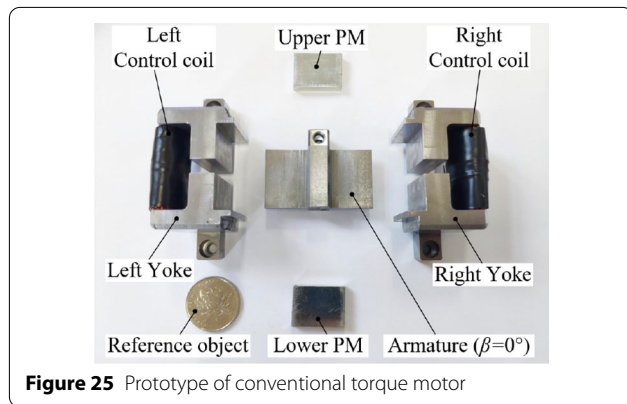
**Figure 24** Magnetic flux densities under different currents and displacements

Table 7 Comparison of magnetic flux densities under different currents and displacements

i (A)		0	0.5	1	1.5
B_1 (T) ($z = 0.6$ mm)	Analytical	0.090	0.139	0.188	0.237
	FEM	0.097	0.141	0.191	0.235
	Experimental	0.095	0.137	0.176	0.216
B_2 (T) ($z = 0.6$ mm)	Analytical	0.188	0.130	0.072	0.015
	FEM	0.198	0.138	0.078	0.021
	Experimental	0.181	0.127	0.069	0.024

**Figure 25** Prototype of conventional torque motor**Table 8** Comparison of output torques between REMC-NFM and torque motor

	$K_t i$ (N·m) ($\theta = 0^\circ$)		$K_{mr} \theta$ (N·m) ($i = 0$ A)	
	$i = 0.5$ A	$i = 1$ A	$\theta = 0.3^\circ$	$\theta = 0.6^\circ$
REMC-NFM	0.101	0.208	0.017	0.033
Torque motor	0.138	0.278	0.035	0.077
Theoretical ratio (Eqs. (44) and (45))	0.707	0.707	0.5	0.5
Experimental ratio	0.732	0.748	0.486	0.429
Difference (%)	3.4	5.5	2.8	14.2

shown in Figure 25. Experiment of torque-angle characteristics of torque motor are performed. And the results are compared with counterparts of REMC-NFM, as shown in Table 8. When the current is 1 A and the rotation angle is 0° , the theoretical ratio of the output torques between these two EMCs is 0.707, while the experimental ratio is 0.748, where the difference is 5.5%. When the current is 0 A and the rotation angle is 0.6° , the theoretical ratio of the output torques between these two EMCs is 0.45, and the experimental ratio is 0.429, where the difference is 14.2%. This conclusion basically conforms to the qualitative analysis of $K_t i$ and

$K_{mr} \theta$ in Eqs. (44) and (45), which validates the correctness of these formulas.

7 Conclusions

- (1) In order to replace the feedback mechanism of spiral groove and thus reduce cost of valve manufacturing, this paper presents a novel configuration of rotary electro-mechanical converter with negative feedback mechanism (REMC-NFM).
- (2) To rapidly and quantitative evaluate the driving and feedback performance, an accurate analytical model of REMC-NFM is proposed, which takes the magnetic leakage effect of PMs and control coils, the edge effect of the air gaps, and the nonlinearity of permeability into account. The experimental results are used to validate the analytical results, which verifies the correctness of the analytical model.
- (3) For qualitative analysis the analytical model is properly simplified, which shows that the torque of REMC-NFM consists of three parts those are related to current, armature rotation and armature displacement, respectively. Based on simplified model, the optimal pitch angle of REMC-NFM is obtained.
- (4) The prototype of REMC-NFM is manufactured and relevant experiments are performed. For torque-angle characteristics, the overall torque increases with both current and rotation angle, which reaches about 0.48 N·m with 1.5 A and 1.5° . While for torque-displacement characteristics, the overall torque increases with current yet decrease with armature displacement due to the feedback mechanism, which is about 0.16 N·m with 1.5 A and 0.8 mm.
- (5) Experiment of torque-angle characteristics of torque motor are performed. And the results are compared with counterparts of REMC-NFM. This conclusion basically conforms to the qualitative analysis of $K_t i$ and $K_{mr} \theta$ in Eqs. (44) and (45), which validates the correctness of these formulas.
- (6) The research indicates that the REMC-NFM can be potentially used as the electro-mechanical converter for 2D valves in civil servo areas. In the future research, the REMC-NFM needs to be connected with 2D valve body, therefore the whole valve characteristics can be explored.

Appendix

Substituting Eqs. (6), (9), (10), (12)–(15), (17)–(20) into Eq. (21), the magnetic flux density B_1 on the magnetic flux strengthening side and the magnetic flux B_2 on the magnetic flux weakening side can be obtained:

$$\begin{aligned}
 B_1 = B_3 = & (l_m \delta N_c i / \mu_m A_m + M l_c \gamma / \mu_2 A_{yc} + 2 l_{ar} \gamma \delta N_c i / \mu_1 A_{ar} + (l_{yp} / \mu_2 A_{yp} \\
 & + 1 / (\mu_0 A_g / (g + x) + 0.78 \mu_0 L_{g1} + 1.04 \mu_0 L_{g2} + \mu_0 L_{g1} \ln(1 + 2m / (g + x)) \\
 & / \pi + 2 \mu_0 (L_{g1} - 2 L_{g2}) \ln(1 + m / (g + x)) / \pi + 0.308 \mu_0 (g + x) + \mu_0 m)) \\
 & (2 \gamma \delta N_c i + 2 \gamma \delta M)) / (l_{yc} l_m / \mu_2 A_{yc} \mu_m A_m + 2 l_{yc} l_{ar} \gamma / \mu_2 A_{yc} \mu_1 A_{ar} \\
 & + (2 l_{yp} / \mu_2 A_{yp} + 1 / (\mu_0 A_g / (g - x) + 0.78 \mu_0 L_{g1} + 1.04 \mu_0 L_{g2} \\
 & + \mu_0 L_{g1} \ln(1 + 2m / (g - x)) / \pi + 2 \mu_0 (L_{g1} - 2 L_{g2}) \ln(1 + m / (g - x)) / \pi \\
 & + 0.308 \mu_0 (g - x) + \mu_0 m) + 1 / (\mu_0 A_g / (g + x) + 0.78 \mu_0 L_{g1} \\
 & + 1.04 \mu_0 L_{g2} + \mu_0 L_{g1} \ln(1 + 2m / (g + x)) / \pi + 2 \mu_0 (L_{g1} - 2 L_{g2}) \\
 & \ln(1 + m / (g + x)) / \pi + 0.308 \mu_0 (g + x) + \mu_0 m)) (l_m \delta / \mu_m A_m + l_{yc} \gamma / \mu_2 A_{yc} \\
 & + 2 l_{ar} \gamma \delta / \mu_1 A_{ar}) + 4 \gamma \delta (l_{yp} / \mu_2 A_{yp} + 1 / (\mu_0 A_g / (g - x) + 0.78 \mu_0 L_{g1} \\
 & + 1.04 \mu_0 L_{g2} + \mu_0 L_{g1} \ln(1 + 2m / (g - x)) / \pi + 2 \mu_0 (L_{g1} - 2 L_{g2}) \\
 & \ln(1 + m / (g - x)) / \pi + 0.308 \mu_0 (g - x) + \mu_0 m)) (l_{yp} / \mu_2 A_{yp} \\
 & + 1 / (\mu_0 A_g / (g + x) + 0.78 \mu_0 L_{g1} + 1.04 \mu_0 L_{g2} + \mu_0 L_{g1} \ln(1 + 2m / (g + x)) \\
 & / \pi + 2 \mu_0 (L_{g1} - 2 L_{g2}) \ln(1 + m / (g + x)) / \pi + 0.308 \mu_0 (g + x) + \mu_0 m))) \\
 & \times (\mu_0 A_g / (g - x)) / (\mu_0 A_g / (g - x) + 0.78 \mu_0 L_{g1} + 1.04 \mu_0 L_{g2} \\
 & + \mu_0 L_{g1} \ln(1 + 2m / (g - x)) / \pi + 2 \mu_0 (L_{g1} - 2 L_{g2}) \ln(1 + m / (g - x)) \\
 & / \pi + 0.308 \mu_0 (g - x) + \mu_0 m) A_g,
 \end{aligned} \tag{48}$$

$$\begin{aligned}
 B_2 = B_4 = & l_m \delta N_c i / \mu_m A_m - M l_c \gamma / \mu_2 A_{yc} + 2 l_{ar} \gamma \delta N_c i / \mu_1 A_{ar} + (l_{yp} / \mu_2 A_{yp} \\
 & + 1 / (\mu_0 A_g / (g - x) + 0.78 \mu_0 L_{g1} + 1.04 \mu_0 L_{g2} + \mu_0 L_{g1} \ln(1 + 2m / (g - x)) \\
 & / \pi + 2 \mu_0 (L_{g1} - 2 L_{g2}) \ln(1 + m / (g - x)) / \pi + 0.308 \mu_0 (g - x) + \mu_0 m)) (2 \gamma \delta N_c i - 2 \gamma \delta M) \\
 & / (l_{yc} l_m / \mu_2 A_{yc} \mu_m A_m + 2 l_{yc} l_{ar} \gamma / \mu_2 A_{yc} \mu_1 A_{ar} + (2 l_{yp} / \mu_2 A_{yp} + 1 / (\mu_0 A_g / (g - x) \\
 & + 0.78 \mu_0 L_{g1} + 1.04 \mu_0 L_{g2} + \mu_0 L_{g1} \ln(1 + 2m / (g - x)) / \pi + 2 \mu_0 (L_{g1} - 2 L_{g2}) \ln(1 + m / (g - x)) / \pi \\
 & + 0.308 \mu_0 (g - x) + \mu_0 m) + 1 / (\mu_0 A_g / (g + x) + 0.78 \mu_0 L_{g1} + 1.04 \mu_0 L_{g2} \\
 & + \mu_0 L_{g1} \ln(1 + 2m / (g + x)) / \pi + 2 \mu_0 (L_{g1} - 2 L_{g2}) \ln(1 + m / (g + x)) / \pi \\
 & + 0.308 \mu_0 (g + x) + \mu_0 m)) (l_m \delta / \mu_m A_m + l_{yc} \gamma / \mu_2 A_{yc} + 2 l_{ar} \gamma \delta / \mu_1 A_{ar}) \\
 & + 4 \gamma \delta (l_{yp} / \mu_2 A_{yp} + 1 / (\mu_0 A_g / (g - x) + 0.78 \mu_0 L_{g1} + 1.04 \mu_0 L_{g2} + \mu_0 L_{g1} \ln(1 + 2m / (g - x)) / \pi \\
 & + 2 \mu_0 (L_{g1} - 2 L_{g2}) \ln(1 + m / (g - x)) / \pi + 0.308 \mu_0 (g - x) + \mu_0 m)) (l_{yp} / \mu_2 A_{yp} \\
 & + 1 / (\mu_0 A_g / (g + x) + 0.78 \mu_0 L_{g1} + 1.04 \mu_0 L_{g2} + \mu_0 L_{g1} \ln(1 + 2m / (g + x)) / \pi \\
 & + 2 \mu_0 (L_{g1} - 2 L_{g2}) \ln(1 + m / (g + x)) / \pi + 0.308 \mu_0 (g + x) + \mu_0 m))) \\
 & \times (\mu_0 A_g / (g + x)) / (\mu_0 A_g / (g + x) + 0.78 \mu_0 L_{g1} + 1.04 \mu_0 L_{g2} \\
 & + \mu_0 L_{g1} \ln(1 + 2m / (g + x)) / \pi + 2 \mu_0 (L_{g1} - 2 L_{g2}) \\
 & \ln(1 + m / (g + x)) / \pi + 0.308 \mu_0 (g + x) + \mu_0 m) A_g.
 \end{aligned} \tag{49}$$

Substituting Eqs. (47) and (48) into Eq. (23) can get the output torque T :

$$\begin{aligned}
 T = & ((l_m \delta N_c i / \mu_m A_m + M l_c \gamma / \mu_2 A_{yc} + 2 l_{ar} \gamma \delta N_c i / \mu_1 A_{ar} + (l_{yp} / \mu_2 A_{yp} + 1 / (\mu_0 A_g / (g + x) \\
 & + 0.78 \mu_0 L_{g1} + 1.04 \mu_0 L_{g2} + \mu_0 L_{g1} \ln(1 + 2m / (g + x)) / \pi \\
 & + 2 \mu_0 (L_{g1} - 2L_{g2}) \ln(1 + m / (g + x)) / \pi + 0.308 \mu_0 (g + x) + \mu_0 m)) (2 \gamma \delta N_c i \\
 & + 2 \gamma \delta M)) / (l_{yc} l_m / \mu_2 A_{yc} \mu_m A_m + 2 l_{yc} l_{ar} \gamma / \mu_2 A_{yc} \mu_1 A_{ar} \\
 & + (2 l_{yp} / \mu_2 A_{yp} + 1 / (\mu_0 A_g / (g - x) + 0.78 \mu_0 L_{g1} \\
 & + 1.04 \mu_0 L_{g2} + \mu_0 L_{g1} \ln(1 + 2m / (g - x)) / \pi \\
 & + 2 \mu_0 (L_{g1} - 2L_{g2}) \ln(1 + m / (g - x)) / \pi \\
 & + 0.308 \mu_0 (g - x) + \mu_0 m) + 1 / (\mu_0 A_g / (g + x) + 0.78 \mu_0 L_{g1} \\
 & + 1.04 \mu_0 L_{g2} + \mu_0 L_{g1} \ln(1 + 2m / (g + x)) / \pi + 2 \mu_0 (L_{g1} - 2L_{g2}) \ln \\
 & (1 + m / (g + x)) / \pi + 0.308 \mu_0 (g + x) + \mu_0 m)) (l_m \delta / \mu_m A_m + l_{yc} \gamma / \mu_2 A_{yc} \\
 & + 2 l_{ar} \gamma \delta / \mu_1 A_{ar} + 4 \gamma \delta (l_{yp} / \mu_2 A_{yp} + 1 / (\mu_0 A_g / (g - x) + 0.78 \mu_0 L_{g1} \\
 & + 1.04 \mu_0 L_{g2} + \mu_0 L_{g1} \ln(1 + 2m / (g - x)) / \pi + 2 \mu_0 (L_{g1} - 2L_{g2}) \\
 & \ln(1 + m / (g - x)) / \pi + 0.308 \mu_0 (g - x) + \mu_0 m)) (l_{yp} / \mu_2 A_{yp} \\
 & + 1 / (\mu_0 A_g / (g + x) + 0.78 \mu_0 L_{g1} + 1.04 \mu_0 L_{g2} + \mu_0 L_{g1} \\
 & \ln(1 + 2m / (g + x)) / \pi + 2 \mu_0 (L_{g1} - 2L_{g2}) \ln(1 + m / (g + x)) / \pi \\
 & + 0.308 \mu_0 (g + x) + \mu_0 m)) \times (\mu_0 A_g / (g - x)) / (\mu_0 A_g / (g - x) + 0.78 \mu_0 L_{g1} \\
 & + 1.04 \mu_0 L_{g2} + \mu_0 L_{g1} \ln(1 + 2m / (g - x)) / \pi + 2 \mu_0 (L_{g1} - 2L_{g2}) \ln(1 + m / (g - x)) / \pi \\
 & + 0.308 \mu_0 (g - x) + \mu_0 m))^2 - (l_m \delta N_c i / \mu_m A_m - M l_c \gamma / \mu_2 A_{yc} \\
 & + 2 l_{ar} \gamma \delta N_c i / \mu_1 A_{ar} + (l_{yp} / \mu_2 A_{yp} + 1 / (\mu_0 A_g / (g - x) \\
 & + 0.78 \mu_0 L_{g1} + 1.04 \mu_0 L_{g2} + \mu_0 L_{g1} \ln(1 + 2m / (g - x)) / \pi \\
 & + 2 \mu_0 (L_{g1} - 2L_{g2}) \ln(1 + m / (g - x)) / \pi + 0.308 \mu_0 (g - x) + \mu_0 m)) \\
 & (2 \gamma \delta N_c i - 2 \gamma \delta M)) / (l_{yc} l_m / \mu_2 A_{yc} \mu_m A_m \\
 & + 2 l_{yc} l_{ar} \gamma / \mu_2 A_{yc} \mu_1 A_{ar} + (2 l_{yp} / \mu_2 A_{yp} + 1 / (\mu_0 A_g / (g - x) + 0.78 \mu_0 L_{g1} \\
 & + 1.04 \mu_0 L_{g2} + \mu_0 L_{g1} \ln(1 + 2m / (g - x)) / \pi \\
 & + 2 \mu_0 (L_{g1} - 2L_{g2}) \ln(1 + m / (g - x)) / \pi + 0.308 \mu_0 (g - x) + \mu_0 m) \\
 & + 1 / (\mu_0 A_g / (g + x) + 0.78 \mu_0 L_{g1} + 1.04 \mu_0 L_{g2} + \mu_0 L_{g1} \ln(1 + 2m / (g + x)) / \pi \\
 & + 2 \mu_0 (L_{g1} - 2L_{g2}) \ln(1 + m / (g + x)) / \pi + 0.308 \mu_0 (g + x) + \mu_0 m)) \\
 & (l_m \delta / \mu_m A_m + l_{yc} \gamma / \mu_2 A_{yc} + 2 l_{ar} \gamma \delta / \mu_1 A_{ar} + 4 \gamma \delta (l_{yp} / \mu_2 A_{yp} + 1 / (\mu_0 A_g / (g - x) \\
 & + 0.78 \mu_0 L_{g1} + 1.04 \mu_0 L_{g2} + \mu_0 L_{g1} \ln(1 + 2m / (g - x)) / \pi \\
 & + 2 \mu_0 (L_{g1} - 2L_{g2}) \ln(14 \gamma \delta (l_{yp} / \mu_2 A_{yp} + 1 / (\mu_0 A_g / (g - x) + 0.78 \mu_0 L_{g1} + 1.04 \mu_0 L_{g2} \\
 & + \mu_0 L_{g1} \ln(1 + 2m / (g - x)) / \pi + 2 \mu_0 (L_{g1} - 2L_{g2}) \ln(1 + m / (g - x)) / \pi \\
 & + 0.308 \mu_0 (g - x) + \mu_0 m)) (l_{yp} / \mu_2 A_{yp} + 1 / (\mu_0 A_g / (g + x) + 0.78 \mu_0 L_{g1} \\
 & + 1.04 \mu_0 L_{g2} + \mu_0 L_{g1} \ln(1 + 2m / (g + x)) / \pi + 2 \mu_0 (L_{g1} - 2L_{g2}) \\
 & \ln(1 + m / (g + x)) / \pi + 0.308 \mu_0 (g + x) + \mu_0 m)) \times (\mu_0 A_g / (g + x)) / (\mu_0 A_g / (g + x) + 0.78 \mu_0 L_{g1} \\
 & + 1.04 \mu_0 L_{g2} + \mu_0 L_{g1} \ln(1 + 2m / (g + x)) / \pi + 0.308 \mu_0 (g + x) + \mu_0 m))^2) \cos \beta / \mu_0 A_g.
 \end{aligned} \tag{50}$$

Acknowledgements

Not applicable.

Authors' contributions

BM, JR and CD were in charge of the whole paper; Dr. BM wrote the manuscript; MD was in charge of analysis modelling and experiments. CHZ and CCZ was in charge of FEM simulation. All authors read and approved the final manuscript.

Authors' Information

Bin Meng, born in 1979, is currently an associate professor and a PhD candidate supervisor at College of Mechanical Engineering, Zhejiang University of Technology, China. He received his PhD degree from Zhejiang University of Technology, China, in 2013. His main research interests include electro-mechanical converters, fluid power transmission and control, and novel hydraulic components.

Mingzhu Dai, born in 1997, is currently a master candidate at Zhejiang University of Technology, China.

Chenhang Zhu, born in 1997, is currently a master candidate at Zhejiang University of Technology, China.

Chenchen Zhang, born in 1996, is currently a master candidate at Zhejiang University of Technology, China.

Chuan Ding, born in 1986, is currently a lecturer and a MSc candidate supervisor at College of Mechanical Engineering, Zhejiang University of Technology, China. His main research interests include mechatronics engineering, fluid power transmission and control, ocean engineering.

Jian Ruan, born in 1963, is a professor and a PhD candidate supervisor at College of Mechanical Engineering, Zhejiang University of Technology, China. He received his PhD degree from Harbin Institute of Technology, China, in 1989. His main research interests include fluid power transmission and novel hydraulic components.

Funding

Supported by National Natural Science Foundation of China (Grant Nos. 51975524, 51405443) and National Key Research and Development Program of China (Grant No. 2019YFB2005200).

Competing interests

The authors declare no competing financial interests.

Received: 7 February 2021 Revised: 23 October 2021 Accepted: 14 July 2022

Published online: 24 September 2022

References

- [1] H Y Yang. Review of Intelligent Manufacturing and Intelligent Hydraulic Components. *Chinese Hydraulic & Pneumatics*, 2020, (1): 1–9. (in Chinese)
- [2] P Tamburrano, A R Plummer, E Distaso, et al. A review of electro-hydraulic servovalve research and development. *International Journal of Fluid Power*, 2018: 1–23. <https://doi.org/10.1080/14399776.2018.1537456>.
- [3] P Tamburrano, A R Plummer, E Distaso. A review of direct drive proportional electrohydraulic spool valves: industrial state-of-the-art and research advancements. *Journal of Dynamic Systems, Measurement, and Control*, 2019, 141(2): 020801.
- [4] J J Vyas, B Gopalsamy, H Joshi. *Electro-hydraulic actuation systems: Design, testing, identification and validation*. Singapore: Springer Press, 2018.
- [5] B Xu, J Shen, S H Liu, et al. Research and development of electro-hydraulic control valves oriented to Industry 4.0: A review. *Chinese Journal of Mechanical Engineering*, 2020, 33: 29. <https://doi.org/10.1186/s10033-020-00446-2>.
- [6] Y B Yin. *Electro hydraulic control theory and its applications under extreme environment*. Oxford: Butterworth-Heinemann, 2019.
- [7] R Amirante, E Distaso, P Tamburrano. Sliding spool design for reducing the actuation forces in direct operated proportional directional valves: Experimental validation. *Energy Conversion and Management*, 2016, 119: 399–410.
- [8] S Z Zhang, N Z Aung, S J Li. Reduction of undesired lateral forces acting on the flapper of a flapper–nozzle pilot valve by using an innovative flapper shape. *Energy Conversion and Management*, 2015, 106: 835–848.
- [9] N Z Aung, Q J Yang, M Chen, et al. CFD analysis of flow forces and energy loss characteristics in a flapper–nozzle pilot valve with different null clearances. *Energy Conversion and Management*, 2014, 83: 284–295.
- [10] H Yang, W Wang, K Q Lu, et al. Cavitation reduction of a flapper–nozzle pilot valve using continuous microjets. *International Journal of Heat and Mass Transfer*, 2019, 133: 1099–1109.
- [11] H Yan, F J Wang, C C Li. Research on the jet characteristics of the deflector–jet mechanism of the servo valve. *Chinese Physics B*, 2017, 26(4): 252–260.
- [12] C M Li, Y B Yin, M Y Wang, et al. Influence of high temperature on couples matching and characteristics of jet pipe electrohydraulic servovalve. *Journal of Mechanical Engineering*, 2018, 54(20): 251–261. (in Chinese)
- [13] J Ruan, R Burton, P R Ukrainetz. An investigation into the characteristics of a two dimensional “2D” flow control valve. *Journal of Dynamic Systems Measurement and Control*, 2002, 124(1): 214–220.
- [14] F He, X Chen, P Y Lu, et al. Theoretical analysis and experimental study on two-dimensional cartridge servo valve. *Acta Aeronautica et Astronautica Sinica*, 2019, 40(5): 422590 (in Chinese). <https://doi.org/10.7527/s1000-6893.2018.22590>.
- [15] Y Ren, J Ruan. Theoretical and experimental investigations of vibration waveforms excited by an electro-hydraulic type exciter for fatigue with a two-dimensional rotary valve. *Mechatronics*, 2016, 33: 161–172.
- [16] X Q Zuo, J Ruan, G W Liu, et al. Characteristics of direct-acting airborne 2D electro-hydraulic pressure servo valve. *Acta Aeronautica et Astronautica Sinica*, 2017, 38(11): 421294. (in Chinese)
- [17] Q H Zhang, W Xiong, J Ruan, et al. Research on 2D digital buffering valve for vehicle shift. *Journal of Mechanical Engineering*, 2018, 54(20): 206–212. (in Chinese)
- [18] S Li, J Ruan, B Meng. Two-dimensional electro-hydraulic proportional directional valve. *Journal of Mechanical Engineering*, 2016, 52(2): 202–212. (in Chinese)
- [19] A J Gong. *Research on key technology of moving-coil proportional electromagnet*. China: Zhejiang University, 2016. (in Chinese)
- [20] D Ahn, H Kim, K Choi, et al. Design process of square column-shaped voice coil motor design for magnetic levitation stage. *International Journal of Applied Electromagnetics and Mechanics*, 2020, 62(3): 517–540.
- [21] S Wu, Z X Jiao, L Yan, et al. Development of a direct-drive servo valve with high-frequency voice coil motor and advanced digital controller. *IEEE/ASME Transactions on Mechatronics*, 2014, 19(3): 932–942.
- [22] J Cui, F Ding, Q P Li. Novel bidirectional rotary proportional actuator for electrohydraulic rotary valves. *IEEE Transactions on Magnetics*, 2007, 43(7): 3254–3258.
- [23] J H Buscher, E Amherst. Compilmer: US, 5679989. 1997-10-21 [2021-01-11]. <http://www.pat2pdf.org/patents/pat5679989.pdf>.
- [24] B Meng, Y J Lai, X G Qiu. Regulation method for torque–angle characteristics of rotary electric–mechanical converter based on hybrid air gap. *Chinese Journal of Mechanical Engineering*, 2020, 33: 35. <https://doi.org/10.1186/s10033-020-00452-4>.
- [25] Q F Zhang, L Yan, Z H Duan, et al. High torque density torque motor with hybrid magnetization pole arrays for jet pipe servo valve. *IEEE Transactions on Industrial Electronics*, 2019, 67(3): 2133–2142.
- [26] S Li, Y Song. Dynamic response of a hydraulic servo-valve torque motor with magnetic fluids. *Mechatronics*, 2007, 17(8): 442–447.
- [27] W Zhang, J Peng, S Li. Damping force modeling and suppression of self-excited vibration due to magnetic fluids applied in the torque motor of a hydraulic servovalve. *Energies*, 2017, 10(6): 749. <https://doi.org/10.3390/en10060749>.
- [28] E Urata. Influence of unequal air-gap thickness in servo valve torque motors. *Proceedings of the Institution of Mechanical Engineers, Part C: Journal of Mechanical Engineering Science*, 2007, 221(11): 1287–1297.
- [29] C Liu, H Jiang. Influence of magnetic reluctances of magnetic elements on servo valve torque motors. *Chinese Journal of Mechanical Engineering*, 2016, 29(1): 136–144.
- [30] C Han, S B Choi, Y M Han. A piezoelectric actuator-based direct-drive valve for fast motion control at high operating temperatures. *Applied Sciences*, 2018, 8(10): 1806. <https://doi.org/10.3390/app8101806>.
- [31] Z S Yang, Z B He, F B Yang, et al. Design and analysis of a voltage driving method for electro-hydraulic servo valve based on giant magnetostrictive actuator. *International Journal of Applied Electromagnetics and Mechanics*, 2018, 57(4): 1–18.

- [32] G L Hu, K Y Zheng. Pressure drop and response time analysis of magnetorheological valve with mosquito-plate fluid flow channels. *Transactions of the Chinese Society for Agricultural Machinery*, 2019, 50(10): 401–409. (in Chinese)
- [33] H Shi, B He, Z Wang, et al. Magneto-mechanical behavior of magnetic shape memory alloy and its application in hydraulic valve actuator. *Journal of Mechanical Engineering*, 2018, 54(20): 235–244. (in Chinese)
- [34] B L Wang. *Design basis of electromagnetic appliances*. Beijing: National Defense Industry Press, 1989.

Submit your manuscript to a SpringerOpen[®] journal and benefit from:

- Convenient online submission
- Rigorous peer review
- Open access: articles freely available online
- High visibility within the field
- Retaining the copyright to your article

Submit your next manuscript at ► [springeropen.com](https://www.springeropen.com)
